Settling Velocity of Snow with Varying Morphology in the Atmospheric Turbulence

A DISSERTATION
SUBMITTED TO THE FACULTY OF
UNIVERSITY OF MINNESOTA
BY

Kaeul Lim

IN PARTIAL FULFILLMENT OF THE REQUIREMENTS
FOR THE DEGREE OF
MASTER OF SCIENCE

Advisor: Jiarong Hong

June 2020

Acknowledgements

I would not be where I am today without the help, guidance, and friendship of many people at the University of Minnesota and Saint Anthony Falls Laboratory as well as my friends and family, who supported me along the way.

I am especially grateful to my adviser, Prof. Jiarong Hong, for giving me the chance to find a project that fits my skillset and interest. His enthusiasm for science and optimism about research helped motivate me to push my experiments past what I initially thought was possible. Through him, I have gained insight and perspective to approach scientific research problems and had the opportunity of working on novel in-situ experiments. I consider myself very privileged to have him as my academic advisor who has been guiding, supportive, and encouraging of my freedom to pursue my ideas in the research.

I have had the pleasure of collaborating with a huge number of people who contributed positively to my time at Minnesota. To begin, I would like to thank Prof. Michele Guala who taught me how to search for problems I am passionate about solving and to think critically and deeply about them. I also owe a huge thanks to Prof. Filippo Coletti who advised me to build up useful knowledge in this field. I would like to send my appreciation to my thesis committee, i.e. Professor Filippo Coletti and Professor Michele Guala, for agreeing to serve in the committee and providing useful feedback.

Furthermore, I would like to thank Professor Sungyon Lee and Professor Chris Hogan who have always been inspiring teachers to me and the doors of their offices have been always open for discussion and guidance.

I wouldn’t have been able to work through many of the theoretical and experimental obstacles of my research without the always available support from the Flow Field Imaging Lab; Cheng Li, Aliza Abraham, Zhou Zhou, Buyu Guo, Kevin Mallery, Santosh Kumar, Teja Dasari, Siyao Shao, Linyue Gao.

Finally, I want to thank the numerous friends and family who have supported me along this journey; it would take far too many pages to thank you all properly. Particularly, I want to thank Jakyung Kim, Ameya Waikar, Juyeong Jung, Eunyeng Hong, Jihyeon Mun, Jinsol Choi, Hyesoo Oh, Hyeonseo Song, Junghyun Kim, Sujin Lee, Hyungyeong Lee, Sonhye Shin, Chaeyoung Park, Joohye Park, I consider myself very lucky for having you in my personal and academic life. I sincerely thank my wonderful family for always being there for me through the best and worst of my life. I deeply believe that I would have never reached this goal without their tremendous love, support, and encouragement.

This work was supported financially by the collaborative research of Prof. Guala, Prof. Hong, and Prof. Coletti from the National Science Foundation.

Dedication

To my dearest parents, Jaesung Lim and Sunhwa Jeong, and older brother, Dohyeon Lim who's love, encouragement, and prays of day and night make the most difficult of days bearable.

Abstract

Here we present the field measurements of snow morphology as well as its corresponding settling velocity based on the data collected from multiple deployments at EOLOS Wind Energy Research Field Station at Rosemount, MN, USA. All the deployments were conducted at night, allowing us to implement the in situ large-scale particle image velocimetry (PIV) and particle tracking velocimetry (PTV) to quantify the turbulent flow field and snow particle settling velocity in a sampling area on the order of 10 m as reported by Nemes et al. [J. Fluid Mech. 2017] and Heisel et al. [J. Fluid Mech. 2018]. The general micrometeorological conditions were provided by a 130 m meteorological tower (met-tower) equipped with 4 sonic anemometers and 6 low frequency humidity and temperature sensors at the field site, and the turbulence characteristics were measured using both the met-tower sonics and in situ PIV. In addition, the snow particle size and morphology were captured using digital in-line holography (DIH). Snow particle terminal velocity in quiescent flow is calculated corresponding to the snow morphology based on the modified drag coefficient empirical formulas. The settling velocity of snow particles was captured using in situ PIV or PTV during each deployment. The turbulence conditions from the available deployments varied by an order of magnitude in the Taylor-scale Reynolds number, covering a range of Stokes number and different cases of snow particle-turbulence interaction phenomenology. The snow morphological effect on snow fall speed is quantitatively observed corresponding to the snow particle classification. The comparisons of snow particle fall speed and settling velocity quantify settling velocity enhancement by turbulence. Overall, the presented study focuses on a better understanding of the effects of snow morphology and atmospheric turbulence on the settling velocity of snow in nature.

Table of Contents

List of Figures

List of Tables

Chapter 1: Introduction

Consider a tiny, fragile snow particle falling during winter, drifting gently toward the surface of the earth. When envisioning the fall trajectory of a snow particle, it leads us to expect complex translational and rotational motions, such as side-side oscillations (fluttering) and tumbling. The particle settling motions in turbulent flow have interested scientists for centuries in the study of fluid dynamics and various branches of engineering. Here we focus on investing snow settling dynamics at field scales where natural snowflake motion will be obtained by Particle Image Velocimetry (PIV) and Particle Tracking Velocimetry (PTV), and the morphology of snow particles will be quantified by Digital In-line Holography (DIH). The goal of this study is to develop a predictive understanding of the effects of snow morphology – aggregate, dendrite, graupel, plate, column, needle, and small ice particle – and atmospheric turbulence on the fall speed of snow. Such information is important for developing more accurate models for predicting snow accumulation under various weather conditions.

1.1 Background and motivation

Settling dynamics play a crucial role in the atmospheric phenomena and weather forecasting, which is an indispensable element of human activity. Settling velocity is mainly determined by temperature, turbulence, and particle size and shape (Garret & Yuter 2014). There are still unsolved questions about the settling velocity of irregularly shaped particles in turbulence. Frozen hydrometeors take on all types of shapes and sizes, from graupels to more complicated dendrites and aggregates. Snow particles of various shapes and sizes possess varying masses and dimensions, which influence the aerodynamics of the particles including their fall velocities (Pruppacher & Klett 1997). Quantitative knowledge of the microphysical properties is required for accurate weather and climate predictions, though these properties are not well understood on the scale of individual snow particles.

Different imaging techniques have been developed for imaging snow particle morphology. Lab microscopic imaging is ideal but deviating from real snow particle morphology (Libbrecht 2007). In situ imaging methods are developed as 3D multi-camera imaging (Garrett & Yuter 2014) and digital in-line holography (Nemes *et al.* 2017).

Theoretical calculations are essential for a deeper understanding of the snow particle motions and making meaningful assessments of their roles in cloud microphysical processes. Different shapes of snow particles in motion have different trajectories due to different drag forces, which lead to enhance the still-air terminal velocity compared to spherical particles (Huang & Han 2011; Tran-Cong & Michaelides 2004).

Previous studies have found that the average snowflakes settling velocity in atmospheric turbulence differ from the still-air terminal velocities (Nemes *et al.* 2017; Maxey 1987). The particle-turbulence interaction mechanisms can greatly impact on the settling velocity in turbulence. In specific, the preferential sweeping has a dominant effect leading to settling enhancement because trajectories that sample the downward side of the eddies are favored by the particles (Wang & Maxey 1993).

Investigate canonical flows interacting with spherical microscopic particles or droplets (Alseda *et al.* 2002; Wood, Hwang & Eaton 2005; Ayyalasomayajula *et al.* 2006; Good *et al.* 2014) have qualitatively confirmed many of findings from numerical simulations. There are limitations since it is investigated usually only for ideal cases like homogenous isotropic turbulence interacting with spherical particles. Reynolds numbers relevant to environmental phenomena are hard to obtain in lab experiments unless special measures are taken to reduce the fluid viscosity (Bodenschatz et al. 2010).

Field experiments can reconcile the results from numerical simulations and lab experiments. But field measurements focused on particle-turbulence interaction in the atmosphere are comparatively scarce. This is likely due to the massive range of scales involved, from the particle size to the large-scale motions in shear or convective flows, and consequently the daunting level of resolution and dynamic range needed. Remote observations from radar and satellites are essential to deduce the microphysics cloud structure and the concentration and distribution of aerosols but cannot provide a direct characterization of particle-turbulence interplay. The first direct observation of Lagrangian trajectories and settling velocity of snow particles in the atmospheric surface layer is reported (Nemes *et al.* 2017).

To extend the framework laid out by Nemes *et al.* 2017 and previous studies, the future challenge would have to deal with the factoring of snow morphological and turbulence characteristics and how they influence the physics. This dissertation consists of two major parts of (1) atmospheric turbulence effects on snow settling dynamics and (2) snow morphological effects on snow fall speed. Chapter 2 addresses the properties of atmospheric turbulent flow. In chapter 3, we present snow particle classification and fall velocity models to characterize the aerodynamic properties for irregular snow particles. The thesis concludes with Chapter 4 investigating the effect of turbulence on the fall velocity of snow particles of given morphology. Finally, a summary and future work are addressed in chapter 5.

Chapter 2: Experimental methods for snow settling under atmospheric turbulence

2.1 Experimental setup

2.1.1 Field site

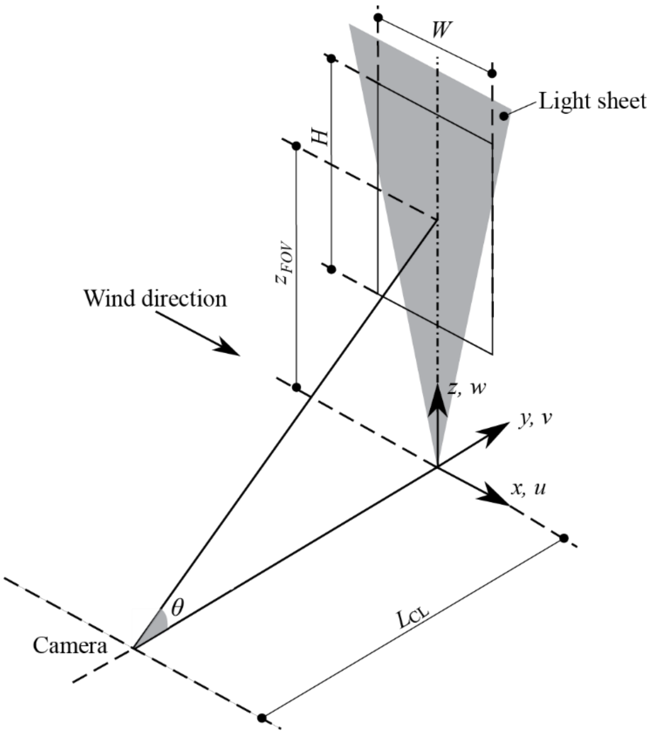

FIGURE 1. Schematic of the measurement setup used in the deployments. Field of view (FOV) geometry defined by the width W, height H, and center field elevation z_{FOV} (see table 1).

The data presented in the current study are from the three field deployments in the period of years 2016 to 2019 as summarized in table 1. The deployments were conducted at Eolos Wind Energy Research Field Station (referred to as the Eolos station hereafter) in Rosemount, MN. The station has a meteorological tower (referred to as the met tower hereafter) to characterize the local atmospheric conditions. The met tower instrumentation includes a number of wind velocity (sonic, cup-and-vane anemometers), temperature and humidity sensors installed at elevations ranging from 7 m to the highest point, 129 m. Four of these elevations (129, 80, 30 and 10 m) are instrumented with high resolution, Campbell

Scientific CSAT3 3D sonic anemometers with a sampling rate of 20 Hz. Three metres below each sonic (elevations of 126, 77, 27 and 7 m) are standard cup-and-vane anemometers with a sampling rate of 1 Hz. Overall, the data from the met tower are sampled continuously 24 hours a day and stored on backed up servers. Details of the research station along with instruments specifications are provided in Hong *et al.* (2014) and Toloui *et al.* (2014).

For each field deployment, the settling dynamics of snow particles is captured using super-large-scale particle image velocimetry (PIV) or particle tracking velocimetry (PTV) described in Hong *et al.* (2014) and Nemes *et al.* (2017), respectively. The corresponding size and shape distribution of snow particles are obtained using in-house digital in-line holographic (DIH) system first introduced in Nemes *et al.* (2017). The meteorological and turbulence conditions according to each deployment are recorded and determined using the data from the met-tower measurements. The key information (e.g. field of view, resolution, and sample size) for PIV/PTV and DIH measurements in each deployment are summarized in table 1 with detailed description of PIV/PTV and DIH presented in the remaining portion of this section. Subsequently, the detailed information regarding the meteorological and turbulence conditions as well as the snow particle conditions are provided in §2.2 and §3.2, respectively.

2.1.2 Large-scale imaging of snow particles

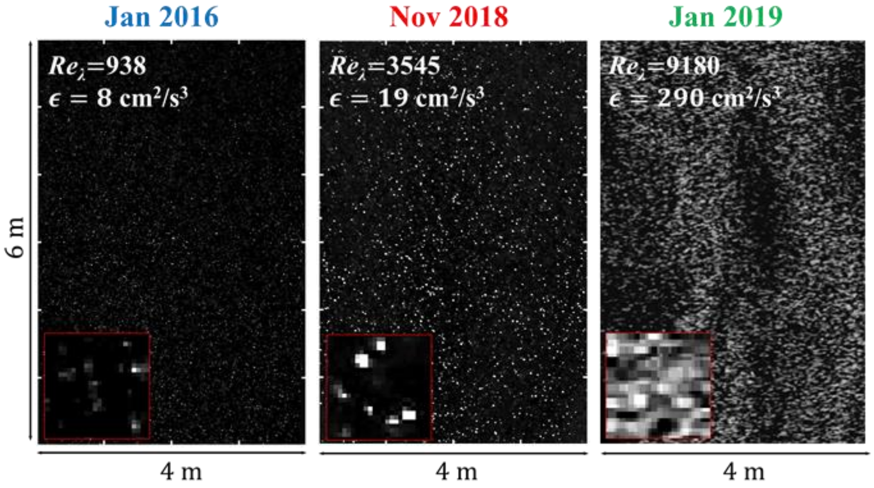

FIGURE 2. (Colour online) Sample acquisition of snow particles zoomed in on a 6×4 m^2 field of view and a 32×32 pixel^2 subset of the image showing individual snow particles.

The general configuration of the experimental setup for PIV/PTV is illustrated in figure 1. The Eulerian and Lagrangian velocity fields were computed using particle image velocimetry (PIV) and particle tracking velocimetry (PTV) respectively. The setup is composed of an optical assembly for illumination, a camera, and the corresponding data acquisition system. The illumination system includes a 5 kW search light (a divergence $< \mathbf{0.3}°$ and an initial beam size of 300 mm in diameter) and a curved reflecting mirror for projecting a horizontal cylindrical beam into a vertical expanding light sheet. The entire system is attached to a trailer for good mobility in aligning the light sheet with the predominant wind direction to ensure out of plane motion within the sampling area is minimized for PIV/PTV. The camera is placed on the ground at a distance of $\boldsymbol{L}_{\mathbf{CL}}$ from the light sheet with a tilted angle $\boldsymbol{\theta}$. The coordinate system (i.e., $\boldsymbol{x}, \boldsymbol{y}, \boldsymbol{z}$ and the corresponding velocity components $\boldsymbol{u}, \boldsymbol{v}, \boldsymbol{w}$) as well as the location and dimensions of field of view (FOV) of PIV/PTV are illustrated in figure 1. Note that the Jan 2016 dataset in table 1 corresponds to the same dataset used in Nemes *et al.* (2017). The Nov 2018 and Jan 2019 datasets are from more recent deployments which yield longer durations of recording under different turbulence and snow particle conditions in comparison to the Jan 2016 dataset. Figure 2 provides sample images of snow particles from each deployment. For comparison of results across different datasets, a sampling region of 7 m × 4 m (matching the field of view of Jan 2016 dataset presented in Nemes *et al.* (2017) with the same 32 pixel × 32 pixel PIV interrogation window is consistent used for all the datasets in the following analyses. Accordingly, both PTV and PIV have been applied to obtain the statistics of snow settling velocity from the Jan 2016 and Nov 2018 datasets, which show consistent results as those demonstrated in (Nemes *et al.*, 2017). In contrast, only PIV is applicable for Jan 2019 dataset due to high particle concentration. Thus, for better comparison across the settling statistics from the datasets with different particle concentrations, the settling velocity are measured in an Eulerian sense inside each interrogation window using PIV. Detailed information including image pre- (e.g. distortion correction) and postprocessing as well as velocity vector calculation for the PTV is available in Nemes *et al.* (2017) and for the PIV can be found in (Dasari, Wu, Liu, & Hong, 2019; Hong *et al.*, 2014; Nemes *et al.*, 2017; Toloui *et al.*, 2014).

2.1.3 Digital holography

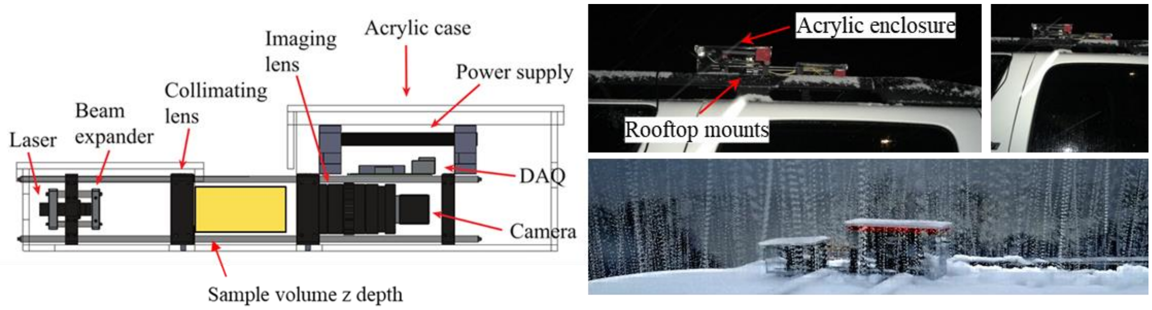

FIGURE 3. The digital in-line holography (DIH) system used to record snowflake images during the field measurements, showing left: schematic of the DIH system, right: mounting on the field vehicle and actual application during a snowfall event.

The size and morphology of snow particles were characterised using digital in-line holography (DIH) in figure 3. The two versions of DIH systems are employed to characterize snow particle morphology (e.g. size and shape) for the three datasets in the present study. The earlier version of DIH was employed for the Jan 2016 dataset and its configuration has been described in detail in Nemes *et al*. (2017). The later version, which has a larger sampling volume with improved spatial resolution and data acquisition capability, was used for the Nov 2018 and Jan 2019 datasets. The later version of DIH uses a diode laser (Roithner 5 mW, 635 nm), a beam expander (Edmund Optics 9 mm plano-concave lens), and a collimating lens (Thorlabs 100 mm biconvex lens with anti-reflective coating) to generate a collimated beam with a 50 mm diameter. It employs a CMOS camera (PtGrey Blackfly 2048 × 1536 pixels, 3.45 µm/pixel) mounted with a Fujinon 25 mm f/1.4 lens to capture the interference pattern between the light scattered from the snowflakes and that from the collimated beam. The camera is connected to the DAQ (Raspberry Pi 3 - Model B), which interfaces with a laptop running FLIR SpinView software to control the camera and collect the images. The entire DIH system is encased in an acrylic enclosure to protect the electronics from moisture. The enclosure contains an opening which is aligned with the mean wind direction to allow the snowflakes to pass through the field of view with minimal disturbance.

	PIV/PTV Setups							DIH Setups		
Deployment datasets	Dataset duration (min)	FOV elevation (z_{FOV}) (m)	FOV size ($H \times W$) (m^2)	Image resolution (mm/pixel)	Mean misalignment angle (deg.)	Camera tilting angle (θ) (deg.)	Camera-to-light distance (L_{CL}) (m)	Image resolution (μm/pixel)	Sample volume (cm^3)	Total number of holograms
Jan 2016	5	10.8	7.1 × 4.0	5.6	10.8	21.1	25	24	18.8	19000
Nov 2018	17	9.1	8.4 × 4.7	6.5	18.5	14.5	31	14	42	51000
Jan 2019	15	20.2	14.7 × 8.3	12.0	8.1	19.9	53	14	42	15312

TABLE 1. Summary of the key parameters of particle image velocimetry (PIV), particle tracking velocimetry (PTV) and digital inline holography (DIH) measurement setups for each deployment dataset used in the present paper (see figure 1). All datasets have the same acquisition rate of 120 fps. Each dataset is referred to by the month and year when the dataset was captured. The Jan 2016 dataset is the same dataset analyzed in Nemes *et al*. (2017). The misalignment angle is defined as the angle between the light sheet and the averaged wind direction.

2.2 Meteorological and turbulence conditions

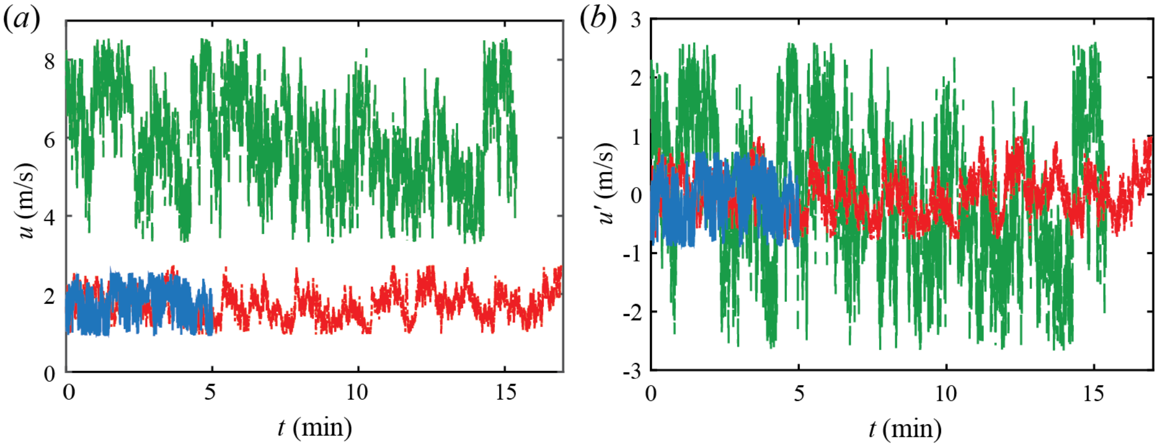

FIGURE 4. (Colour online) Time series of the sonic anemometer data at elevation $z =$ 10 m showing (a) streamwise wind velocity (u) and (b) velocity fluctuation (u') for the Jan 2016 (solid blue line), Nov 2018 (dotted red line), Jan 2019 (dashed green line) datasets.

The meteorological and turbulence conditions during each deployment are characterized using the sonic anemometer measurements from the met tower. In particular, the sonic measurements at z =10 m, which is at the elevation closest to those of PIV/PTV sampling areas, are used to provide a statistical description of the turbulence conditions. As shown in figure 4, the time series of the wind velocity (u) and fluctuation (u') from the 10 m sonic indicates good stationarity of turbulent flow for all the datasets used in the present study. Table 2 summarizes the key meteorological and turbulence parameters for all the datasets. In particular, atmospheric stability conditions are estimated based on both the bulk Richardson number, R_b, and the Obukhov length, L_OB using the formula below

$$R_b = -|g|\Delta\overline{\theta_v}\Delta z/(\overline{\theta_v}[(\Delta U)^2 + (\Delta V)^2]) \tag{1}$$

$$L_{OB} = -{U_\tau}^3\overline{\theta_v}/\kappa g\overline{w'\theta_v'} \tag{2}$$

where $\boldsymbol{g}$ is the gravitational constant, $\boldsymbol{\theta_v}$ is the virtual potential temperature, $\boldsymbol{U}$ and $\boldsymbol{V}$ are the average north and west wind velocity, $\boldsymbol{U_\tau}$ is the shear velocity, $\boldsymbol{w'}$ is the vertical wind velocity fluctuation, and κ is the von K**á**rm**á**n constant. The $\boldsymbol{\theta_v}$ is calculated using 1 Hz temperature, pressure, and relative humidity measurements. The mean velocity difference $\Delta\boldsymbol{U}$ and $\Delta\boldsymbol{V}$ are estimated using difference of velocities measured at the bottom ($\boldsymbol{z}$ =10 m) and top ($\boldsymbol{z}$ =129 m) anemometers, corresponding to $\Delta\boldsymbol{z} = \mathbf{119\ m}$. The $\boldsymbol{L_{OB}}$ is obtained using the sonic anemometer near the surface (i.e. $\boldsymbol{z}$ =10 m). We approximated the surface turbulent virtual potential heat flux as $\overline{\boldsymbol{w}'\boldsymbol{\theta}_{\boldsymbol{v}}{}'}$. The shear velocity, $\boldsymbol{U}_{\boldsymbol{\tau}}$ is characterized based on the Reynolds stress tensor terms $\overline{\boldsymbol{u}'\boldsymbol{w}'}$ and $\overline{\boldsymbol{v}'\boldsymbol{w}'}$ (Stull 1988) using the formula below

$$\boldsymbol{U}_{\boldsymbol{\tau}} = \left(\overline{\boldsymbol{u}'\boldsymbol{w}'}^{\mathbf{2}} + \overline{\boldsymbol{v}'\boldsymbol{w}'}^{\mathbf{2}}\right)^{\mathbf{1/4}} \tag{3}$$

For all the datasets, the values of $\boldsymbol{R}_{\mathbf{b}}$ are close to zero and those of $\boldsymbol{L}_{\mathbf{OB}}$ are significantly larger than the length scales associated with our sampling areas of ~**10 m**, both indicating the atmospheric flows are neutrally stratified (Högström, Hunt & Smedman 2002).

For the turbulence parameters for Jan 2016 data are adopted from Nemes *et al.* (2017). For Nov 2018 and Jan 2019 datasets, the integral time scale, $\boldsymbol{\tau}_{\mathbf{L}}$ is calculated from the temporal auto-correlation function, $\boldsymbol{\rho}$, using the formulas below

$$\rho(\tau) = \langle u'(t)u'(t+\tau)\rangle / {\sigma_{u'}}^2 \tag{4}$$

$$\tau_{\mathrm{L}} = \int_0^{T_0} \rho(\tau)d\tau \tag{5}$$

where τ is the temporal separation, $\sigma_{u'}$ is the standard deviation of u', and T_0 is the 1st zero crossing point of the auto-correlation function. The corresponding integral length scale, L, is obtained via

$$L = \langle u'^2\rangle^{1/2}\tau_{\mathrm{L}} \tag{6}$$

The dissipation rate, ε, is estimated using the second-order temporal streamwise structure function below

$$D_{11}(\tau) \equiv \langle [u'(t+\tau) - u'(t)]^2\rangle \tag{7}$$

To yield better convergence of $D_{11}(\tau)$, the velocity time series are divided into multiple two minutes windows with 50% overlap. The structure function is calculated over each window, and its compensated spatial form (dimensionless) is derived as

$$C_{u'^2}(r) = D_{11}(r)/(\varepsilon\, r)^{2/3} \tag{8}$$

The spatial lag r in the above formula is estimated using Taylor frozen hypothesis as $r = \tau U_{2\mathrm{min}}$ where $U_{2\mathrm{min}}$ is the mean velocity within each two minutes window. The ensemble averaged curve for $C_{u'^2}(r)$ is used to estimate energy dissipation (ε) in the inertial subrange, where it is supposed to reach a plateau according to the Kolmogorov theory (Saddoughi & Veeravalli 1994). As shown in figure 5, the compensated structure function is plotted for the Nov 2018 and Jan 2019 datasets. For both cases, the curve has a constant region with value of 2.0, matching reasonably well with the previous study (e.g., Saddoughi & Veeravalli 1994). Based on the estimate of energy dissipation rate, the corresponding Kolmogorov time and length scale are calculated as $\tau_\eta = \sqrt{\nu/\epsilon}$, and $\eta = (\nu^3/\epsilon)^{1/4}$, and the Taylor microscale $\lambda = \langle u'^2 \rangle^{1/2} \sqrt{15\nu/\epsilon}$ and Taylor microscale Reynolds number $\langle u'^2 \rangle^{1/2} \lambda/\nu$ are also obtained.

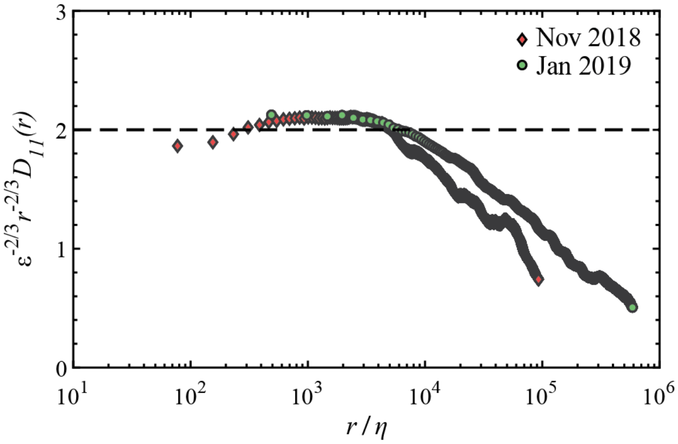

FIGURE 5. The compensated second-order spatial structure function of the streamwise velocity component computed using the sonic measurements at $z = 10$ m. The dashed line corresponds to a constant value of 2.0.

	Meteorological conditions							Turbulence conditions						
Datasets	U (m/s)	σ_u (m/s)	σ_w (m/s)	RH (%)	T (°C)	R_b (–)	L_OB (m)	L (m)	τ_L (s)	ε ($\mathrm{cm}^2/\mathrm{s}^3$)	η (mm)	τ_η (ms)	λ (mm)	Re_λ (–)
Jan 2016	1.98	0.16	0.08	98.3	-0.1	0.03	811	4.9	30.6	8	1.29	126	78	938
Nov 2018	1.55	0.38	0.25	94.3	-1.8	0.12	1007	3.4	8.9	19	1.04	83	122	3545
Jan 2019	5.95	1.18	0.54	80.0	-16.0	0.03	-2643	14.6	12.9	290	0.49	20	93	9180

TABLE 2. The meteorological and turbulence parameters obtained using the sonic anemometer at $z = 10$ m for all three datasets. Here U denotes the mean streamwise wind velocity, σ_u and σ_w the root mean square (r.m.s.) of the streamwise and vertical velocity components, RH relative humidity, T temperature, L the integral length scale, τ_L the integral time scale, ε the dissipation rate, η the Kolmogorov length scale, τ_η the Kolmogorov time scale, λ the Taylor microscale, Re_λ the Taylor microscale Reynolds number, R_b the bulk Richardson number and L_OB the Obukhov length.

Chapter 3: Snow morphology on settling velocity

3.1 Snow particle classification

Snow particles have been classified into various categories throughout history (e.g. Magono & Lee 1966; Mason 1971; Nakaya & Sekido 1936; Libbrecht 2007) based on particle geometrical features. Magono & Lee (1966) classification of snow particles is the most common classifications as shown in figure 6. More recently, snow particles are categorized by riming degree estimation or shape complexity from pictures collected with a MASC (Garret & Yuter 2014; Praz et al. 2017). The wide variety of snow shapes follow snowflakes growth processes including the meteorological condition of temperature and relative humidity (Magono & Lee 1966; Libbrecht 2007) in figure 7.

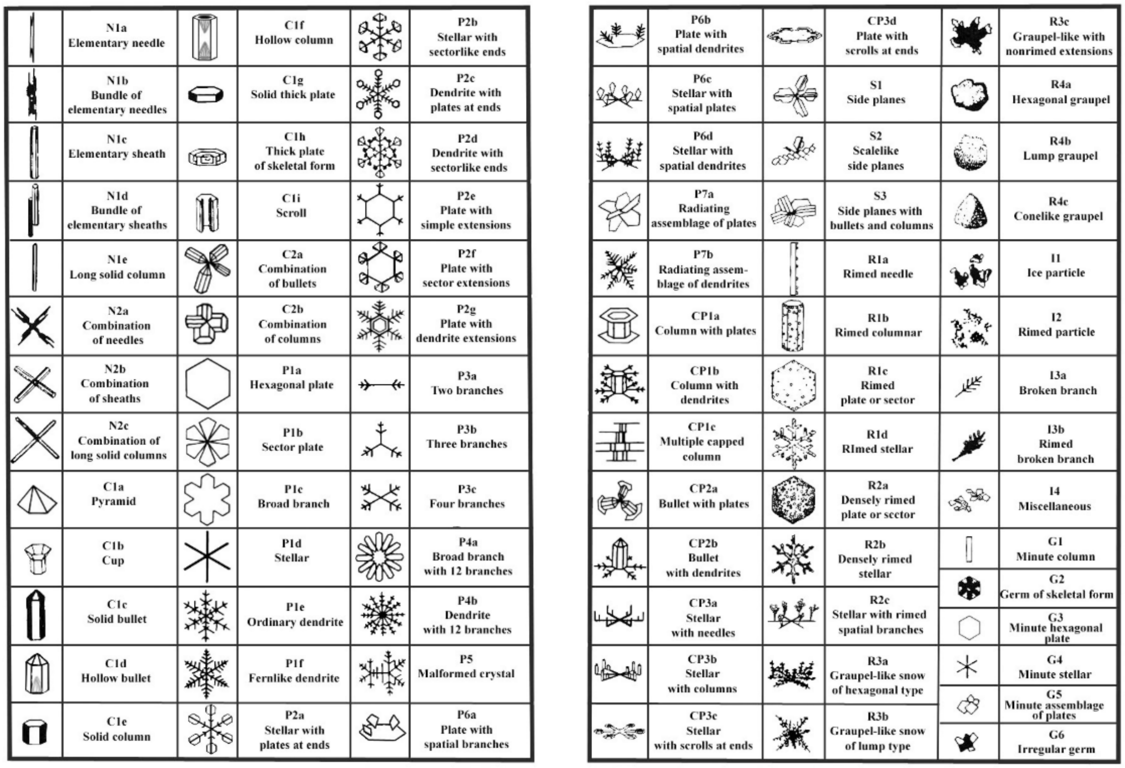

FIGURE 6. Magono-Lee classification of naturally occurring snow crystals from Magono & Lee (1966).

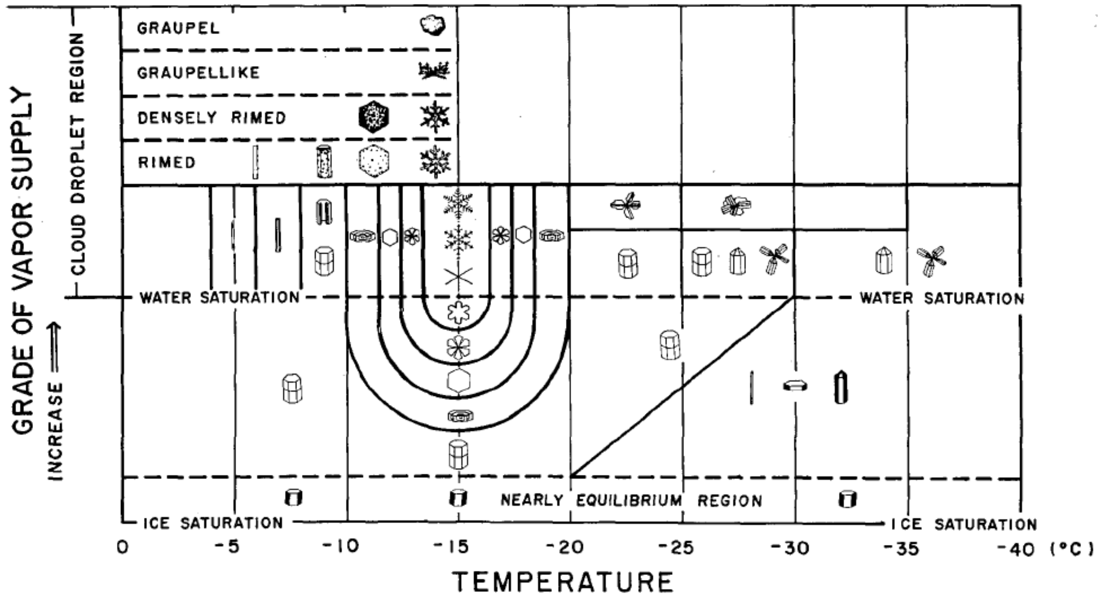

FIGURE 7. Temperature and humidity conditions for the growth of natural snow particles of various types from Magono & Lee (1966).

Having qualitative classification is extremely useful for understanding the descriptive categorization of ice and snow crystals, but these classifications are inadequate for performing physical calculations, which require quantitative classification. There are a handful of possible ways to quantitatively classify frozen hydrometeors. For example, Lim *et al.* (2013) devised a classification methodology of snow particles, such as crystals, aggregates, rimed snow, etc., by utilizing radar reflectivity fields, which can be used for determining more accurate estimates of snowfall rates. The empirical relationships that describe the particle dimensions, diameter, mass, density, and fall velocity are described in §3.2.

Figure 8 depicts the six snow particle types from the DIH system to estimate the still-air particle terminal velocity. We classify snow particles based on the meteorological condition of snow formation, specifically temperature and humidity (Magono & Lee 1966; Libbrecht 2007) and snow geometric features (e.g. particle size and shape). We aim to develop a new snow classification that can meaningfully relate to the physical parameters in snow settling dynamics, typically for the snow fall velocity.

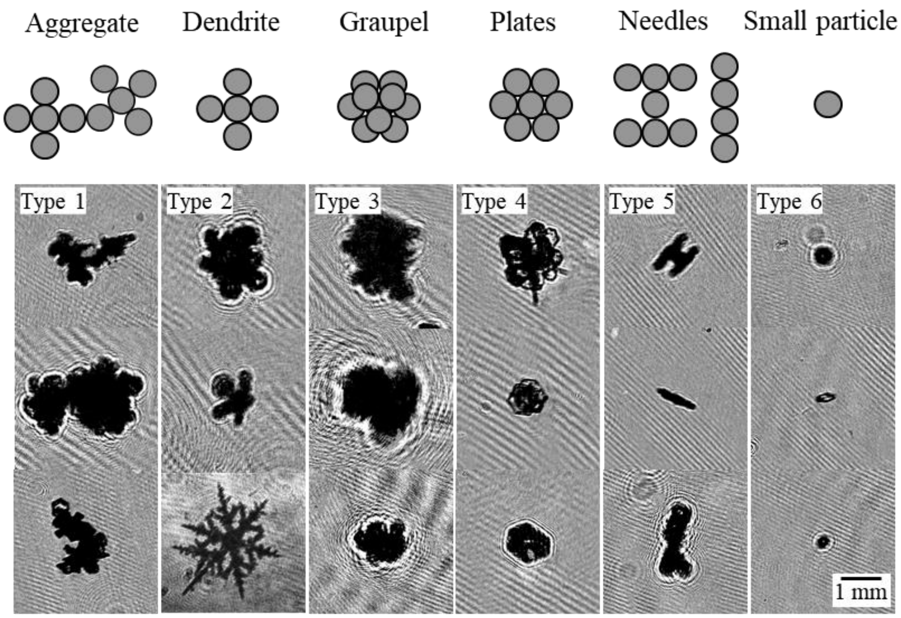

FIGURE 8. The snow particle classification categorized by its geometrical shape and atmospheric snow formation condition: type 1 – aggregates; type 2 – dendrites; type 3 – graupels; type 4 – plates; type 5 – columns and needles; type 6 – small ice particles.

3.2 Snow particle properties

3.3.1 Dimensions and mass

In this section, we describe in detail the information about the snow conditions using the three datasets. Table 3 provides a summary of the snow particle bulk properties characterized using the DIH systems introduced in §2.1. Specifically, as shown in table 3, the size of snow particles is measured using the diameter of projected area corresponding to the diameter of a circle having the same projected area as the snow particle. Snow particle shape is characterized with the aspect ratio defined as the ratio between the major and minor axis of an ellipsoid fit to each particle image detected by the DIH system.

The characteristic parameters for snow particles are defined as follows: S is the effective projected area from the snow holographic image. The cross-sectional area A is defined as the area of ellipsoid with major and minor axis. Figure 9 depicts these definitions graphically.

$$\text{The particle diameter, } d_p = \sqrt{4S/\pi} \tag{9}$$

$$\text{Area ratio, } A_r = S/A \qquad \text{where } A = d_M \times d_m \tag{10}$$

$$\text{Aspect ratio, } E = d_M/d_m \tag{11}$$

$$\text{Sphericity, } \phi = 4\pi S/P^2 \tag{12}$$

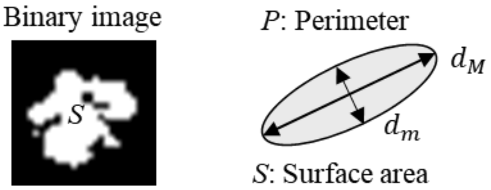

FIGURE 9. Definition of projected area S, perimeter of the projected area, P, and the major axis and minor axis of an ellipsoid fit, respectively d_M and d_m. See text for explanations in detail.

Particle type	Size (d_p) [mm]	Area ratio (A_r) [−]	Aspect ratio (E) [−]	Sphericity (ϕ) [−]
1	1.23±0.36	0.62±0.08	1.94±0.53	0.22±0.13
2	0.67±0.17	0.66±0.09	1.43±0.36	0.32±0.14
3	0.62±0.17	0.72±0.05	1.45±0.30	0.50±0.19
4	0.60±0.22	0.67±0.09	1.37±0.24	0.43±0.18
5	0.56±0.19	0.67±0.09	1.97±0.46	0.44±0.17
6	0.34±0.11	0.57±0.11	1.52±0.47	0.57±0.23

TABLE 3. A summary of snow particle bulk properties characterized using the DIH systems.

Since most of snow particles are not perfectly spherical, a calibration curve was constructed for determining the masses and densities of various snowflakes. The ice particle melting method (Locatelli & Hobbs 1974; Zhang, Pitter & Mitchell 1989) has been used to estimate mass for individual snow particles as a function of diameter. The influence of riming and aggregation on ice particle masses was examined based on the empirical expressions relating snow particle masses and dimensions. The detailed relationships are summarized in Table 4.

Particle type	Mass m [kg]	Density ρ_p [kg/m^3]
1	$0.0029D^{1.9}$	-
2	$0.068D^{2.2}$	-
3	$0.14D^{2.7}$	-
4	$0.028D^{2.5}$	90
5	$0.017{d_M}^{1.8}$	$65{d_M}^{-0.0915}$
6	$0.022D^{2.0}$	-

TABLE 4. A summary of the empirical expressions relating snow particle mass, density, and size.

3.3 Snow particle fall velocity model

The terminal velocity of falling snowflakes has been a topic of interest and debate since the Nakaya & Terada (1935) paper, where the velocity of individual crystals was measured through crystal position observations with the naked eye and the time was measured with a stopwatch. Subsequent studies measured fall velocity using photographic techniques with stroboscopic illumination (e.g., Higuchi 1956, Langleben 1954, Schaefer 1947, Zikmunda & Vali 1972), and radar (e.g., Marshall 1953). The need for accurate predictions of terminal velocity is critical for modeling cloud processes, which have been shown to be sensitive to the parameterization of fall velocities (Starr & Cox 1985).

Snow morphology has a significant impact on snow particle terminal velocity. We predict snow particle fall velocity by a relationship between the Reynolds number (Re) and Best number (X) corresponding to the six classification types respectively, the type 1 aggregate by Heymsfield & Westbrook 2010; type 2 dendrite by Nettesheim & Wang 2018; type 3 graupel by Dioguardi, Mele & Dellino 2018, type 4 plate, type 5 column and needle by Haider & Levenspiel 1989; type 6 small particle by Bohm 1989). Although the five fall velocity models only consider for the idealized snowflakes, it is the first observation of different fall velocity using real snow particles.

Aggregate snow is comprised of a circle, square, hexagram, and pentagram. Heymsfield & Westbrook (2010) proposed adjustment to Michell's (1966) formula, and in all cases, the error is 25 % or less. Although these models are much simplified relative to natural snowflakes, it is a logical first test of aggregate fall velocities. Here ρ_f and η denote the air density and viscosity and g the gravitational acceleration. The procedure for calculating fall velocity, V_t using this method is as follows:

$$X^* = \frac{\rho_f}{\eta^2}\frac{8mg}{\pi A_r^{0.5}} \tag{13}$$

We employ the widely used expression derived by Böhm (1989):

$$Re = \frac{\delta_0^2}{4}\left[\left(1+\frac{4\sqrt{X^*}}{\delta_0^2\sqrt{C_0}}\right)^{1/2}-1\right]^2 \tag{14}$$

With values of the pressure drag coefficient $C_0 = 0.35$ and surface roughness constant $\delta_0 = 8.0$ which were found to provide good agreement with observations of falling aggregate (Mitchell 1996).

$$V_t = \frac{\eta Re}{\rho_f d_p} \tag{15}$$

Nettesheim & Wang (2018) introduced the hydrodynamic behavior of four types of freely falling dendrites through numerical simulations. Fall behavior and an analysis of the results are in general agreement with numerical studies and reported observations. We assume the common feature of dendrite types is broad-branched crystals or stellar crystals, so the fall velocity is estimated as the average value of them:

$$V_t = (1.67\times 10^{-1}{d_p}^{0.265} - 0.59 + 1.87\times 10^{-4}{d_p}^{0.89})/2 \tag{16}$$

Dioguardi, Mele & Dellino (2018) proposed new shape-dependent drag law for graupel type of particles. The particle shapes of graupels are characterized by sphericity and circularity. The terminal velocity is calculated with the new-shape dependent drag law:

$$\text{The unified Davis number, } X = \frac{8mg\rho_f}{\pi\eta^2}\left(\frac{A}{A_e}\right)^{1/4} \tag{17}$$

$$Re = 8.5\left[\left(1+0.1519X^{1/2}\right)^{1/2}-1\right]^2 \tag{18}$$

$$\psi = 4\pi A/P^2 \text{ (Cox, 1927)} \tag{19}$$

$$C_D = \frac{24}{Re}\left(\frac{1-\psi}{Re}+1\right)^{0.25} + \frac{24}{Re}(0.1806Re^{0.6459})\psi^{-(Re^{0.08})} + \frac{0.4251}{1+\frac{6880.96}{Re}\psi^{5.05}} \tag{20}$$

$$V_t = \sqrt{\frac{4gd_p(\rho_p-\rho_f)}{3C_D\rho_f}} \text{ where } \rho_p \text{ is estimated from mass value} \tag{21}$$

Haider & Levenspiel (1989) proposed the fall velocity and diameter relationship for three major particle shapes (sphere, plate and cylinder):

$$\text{The dimensionless diameter } d^* = d_p \left(\frac{g\rho_f(\rho_p-\rho_f)}{\mu^2}\right)^{1/3} \tag{22}$$

$$\text{The dimensionless terminal velocity } V_t^* = \left(\frac{18}{d^{*2}} + \frac{3K_1}{4d^{*0.5}}\right)^{-1} \tag{23}$$

$$\text{where } K_1 = 3.1131 - 2.3252\,\phi$$

$$V_t = V_t^* \left(\frac{\rho_f^2}{g\mu(\rho_p-\rho_f)}\right)^{-1/3} \tag{24}$$

The fall velocity of small particles are derived by the widely used expression from Böhm (1989):

$$V_t = \frac{Re\eta}{2\rho_f d_p} \tag{25}$$

The overall procedure of calculating individual snow particle fall velocities is summarized in figure 10 using the snowflake holographic images from the DIH system.

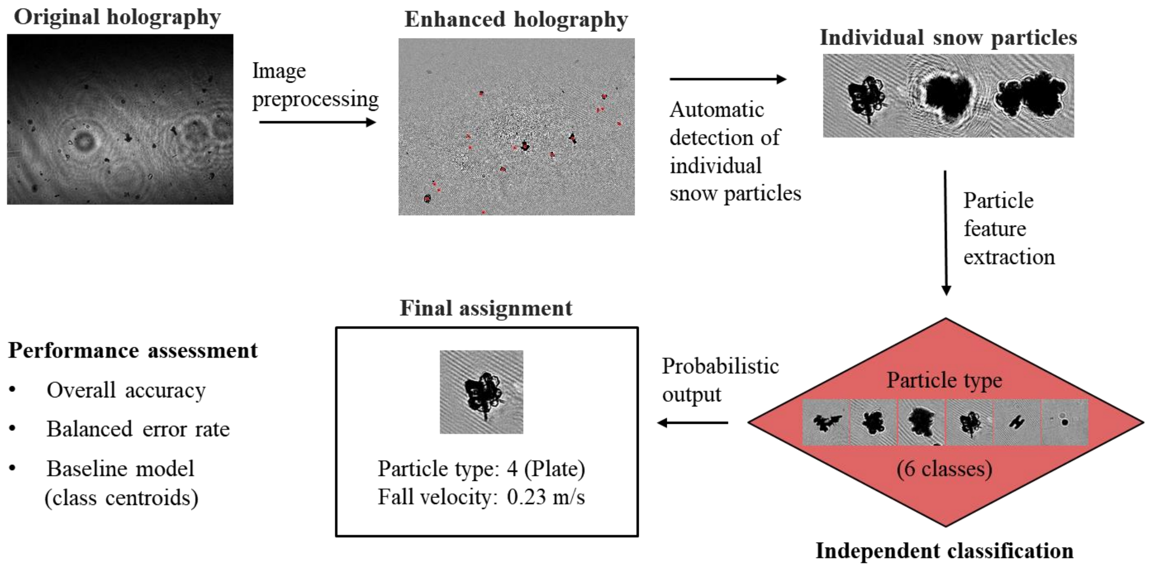

FIGURE 10. Overall procedure to calculate individual snow particle terminal velocities in quiescent flow.

Chapter 4: Results and Discussions

4.1 Snow morphology on snow fall speed

As figure 11 shows, from Jan 2016 to Nov 2018 to Jan 2019 datasets, the average snow particle size reduces with a corresponding decrease in the span of their size distributions (figure 11a) while the snow particle shapes stay close across the three datasets (figure 11b).

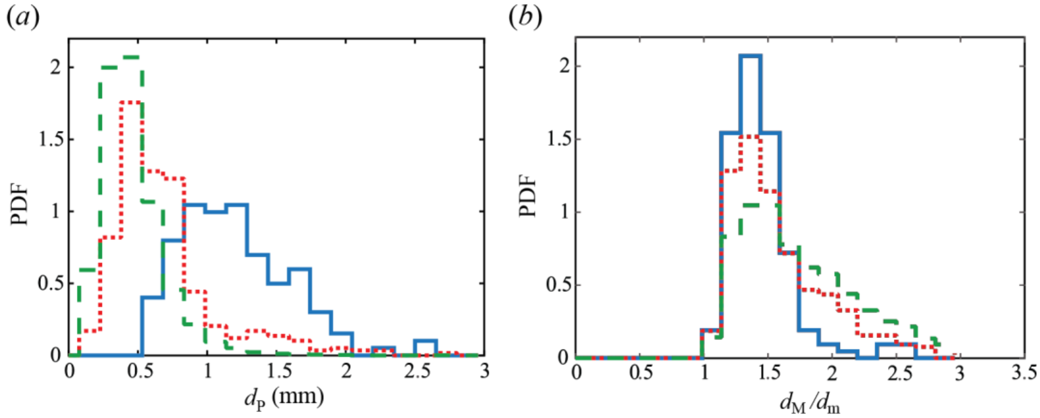

FIGURE 11. The distributions in terms of probability density function (PDF) of (*a*) snow particle size and (*b*) aspect ratio for the Jan 2016 (solid blue line), Nov 2018 (dotted red line), and Jan 2019 (dashed green line) datasets.

The most common type of snow particles is graupel during the three datasets in figure 12. The Nov 2018 dataset includes much more small ice particles compared to other datasets which can influence on the distribution of particle terminal velocity, and the Jan 2019 dataset holds more variety of particle types with type 4 and 5 snowflakes.

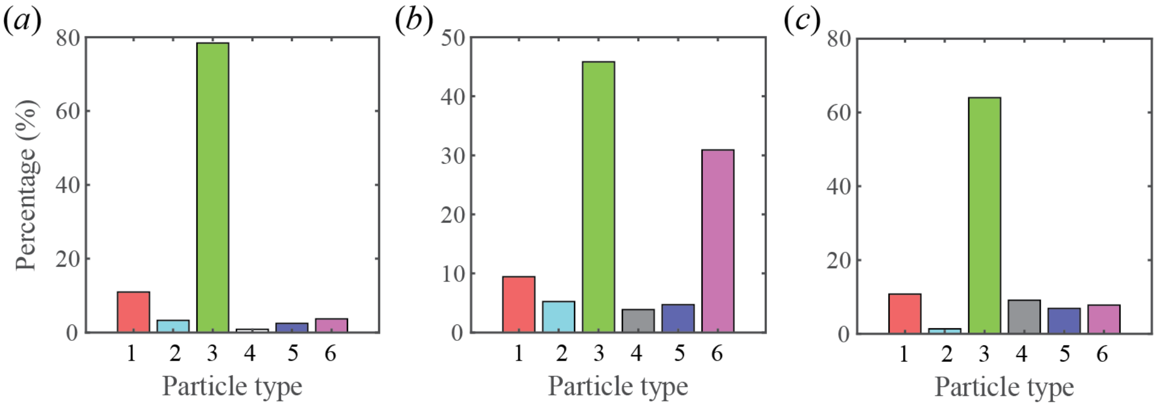

FIGURE 12. The frequency of each snow particle type during the three datasets (*a*) the Jan 2016 (*b*) Nov 2018, and (*c*) Jan 2019 datasets.

The results of freely falling snow particles are presented in this section. Corresponding to each snow categorization, we estimate the still-air particle fall velocity using the five model equations. In figure 13 and 14, the relationship between fall velocity and snow shape are clearly differentiated corresponding to the snow classification types and quantitatively consistent with previous literature (e.g. Garrett & Yuter 2014). The calculated terminal velocities of each particle type can be fit by power law relationships as shown in figure 13. Graupel type has a higher fall velocity which is consistent with previous literature while aggregate type has a smaller value presumably due the difference of particle masses and densities.

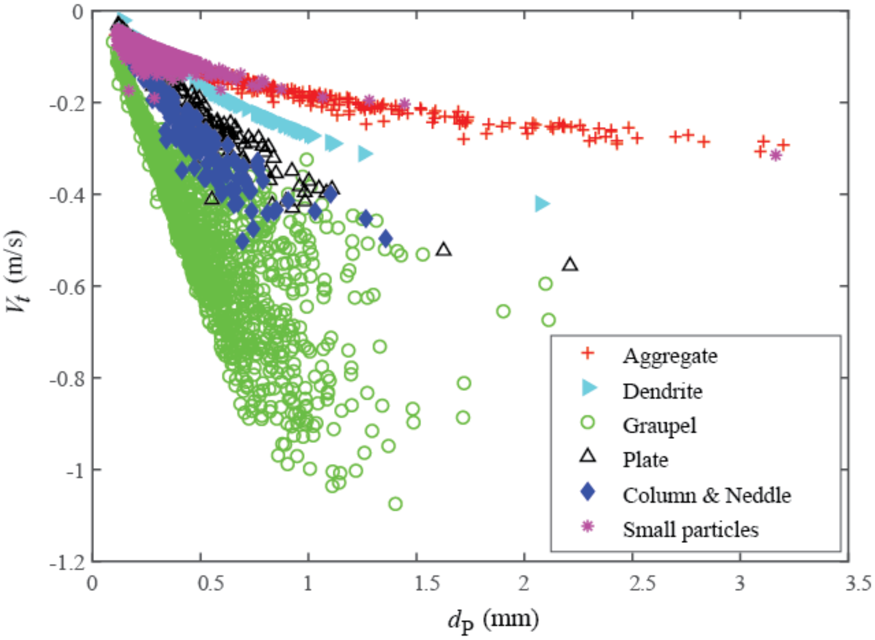

FIGURE 13. Terminal velocities of aggregates, dendrites, graupel, plates, column & needle, and small ice particles from the snowflake holographic images.

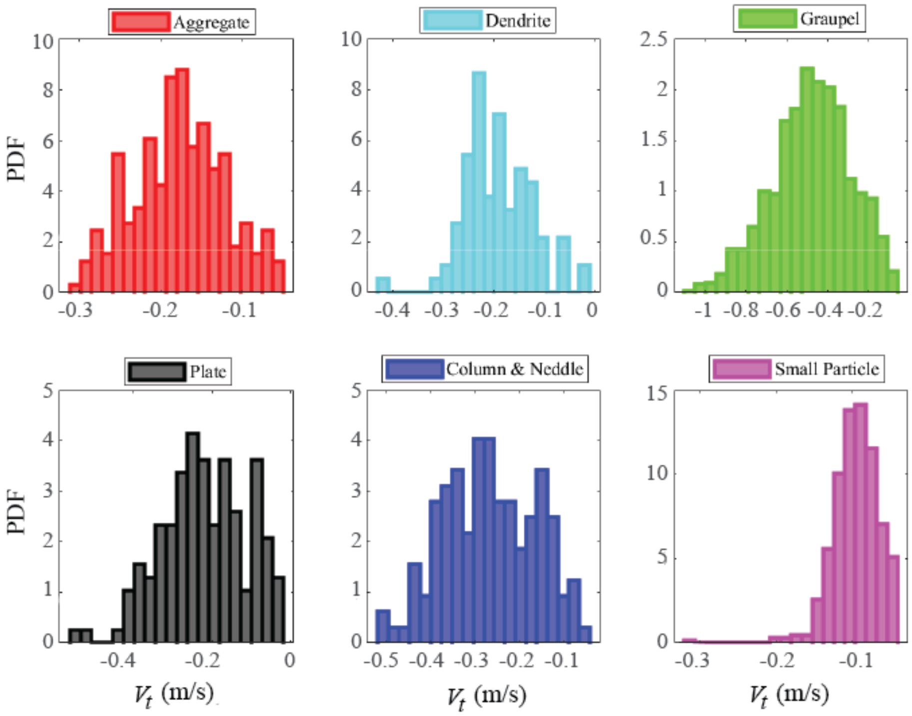

FIGURE 14. Terminal velocity PDFs of aggregates, dendrites, graupel, plates, column & needle, and small ice particles.

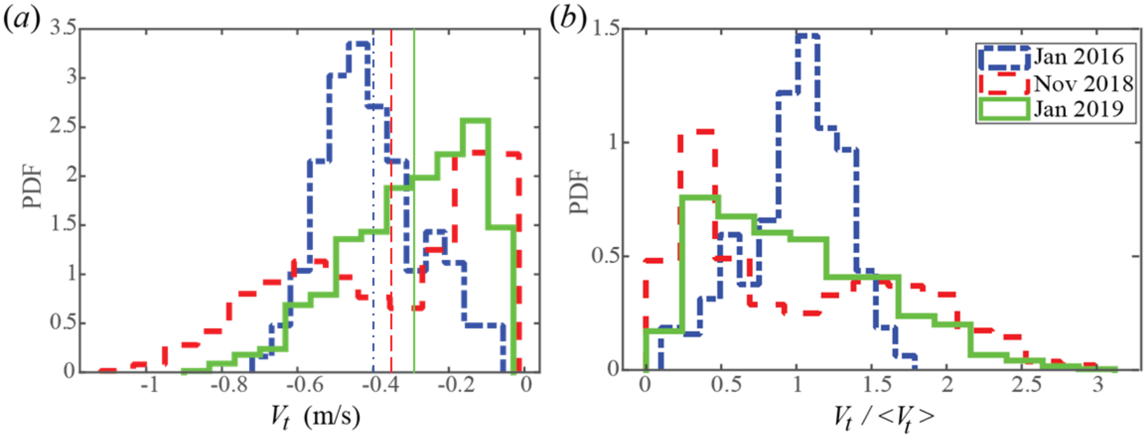

FIGURE 15. (Colour online) (*a*) Snow particle terminal velocity, V_t PDF (*b*) The non-dimensionalized snow particle terminal velocity PDF using average velocity, $< V_t >$ for the Jan 2016 (solid blue line), Nov 2018 (dotted red line), Jan 2019 (dashed green line) datasets.

The still-air particle terminal velocity of snow for all three datasets are used for generating terminal velocity distribution as shown in figure 15(a). The distribution presents a wide range of fall velocities in quiescent flow in terms of the ensemble mean of the fall velocity distribution (table 5) as a result of snow morphological effects. As discussed before, the particle size distribution measured by the DIH system shows a significant difference between three datasets in terms of the mean and standard deviation (see figure 11). Notably, the Jan 2016 and Jan 2019 have the largest and smallest span of particles size distribution, respectively. The mean values of snow particle terminal velocity are correlated with the increasing size of particle diameter from the Jan 2016 to Jan 2019 datasets. The resulting non-dimensionalized distributions in figure 15 exhibit trend in terms of the distribution variance related to the meteorological conditions, especially temperature. Since the Jan 2019 dataset holds very cold temperature, it includes more diverse snow particle morphologies which lead the highest distribution variance.

4.2 Effect of turbulence and snow morphology on snow fall speed

The instantaneous settling velocity of the snow particle denoted as $\boldsymbol{w_s}(\boldsymbol{x}, \boldsymbol{z}, \boldsymbol{t})$ resulting from PIV analysis for all three datasets is used for generating settling velocity distribution, as shown in figure 16. Based on the comparison between the DIH snow fall velocity and the PIV settling velocity distribution, the enhanced snow settling velocity by turbulence was quantitatively observed. However, it is difficult to establish an exact correspondence between the particle conditions characterized using DIH and those for PIV due to different sampling locations of these two measurements (the DIH measurements were performed on the roof of our deployment vehicle near the ground). We also acknowledge that there could be an underestimate of snow particle size due to the sampling bias associated with the location of DIH measurements, particularly for the Jan 2019 dataset which had a higher wind speed and more turbulent flow conditions. For this reason, most of small particles and needles could not be considered at the PIV processing.

Based on the comparison between the snow fall velocity from the DIH system and the PIV settling velocity distribution in figure 16, the enhanced snow settling velocity by turbulence was quantitatively observed (see table 5). For all three datasets, the probability density function (PDF) of the snow particle settling velocity fits well to a normal distribution. The mean values are not fully correlated with the increasing level of turbulence. Its magnitude increases first with increasing turbulence level from Jan 2016 to Nov 2018 datasets, and decreases as the turbulence level further increase in Jan 2018 dataset causing a significant portion of instantaneous velocity shifting to positive values (pointing upward).

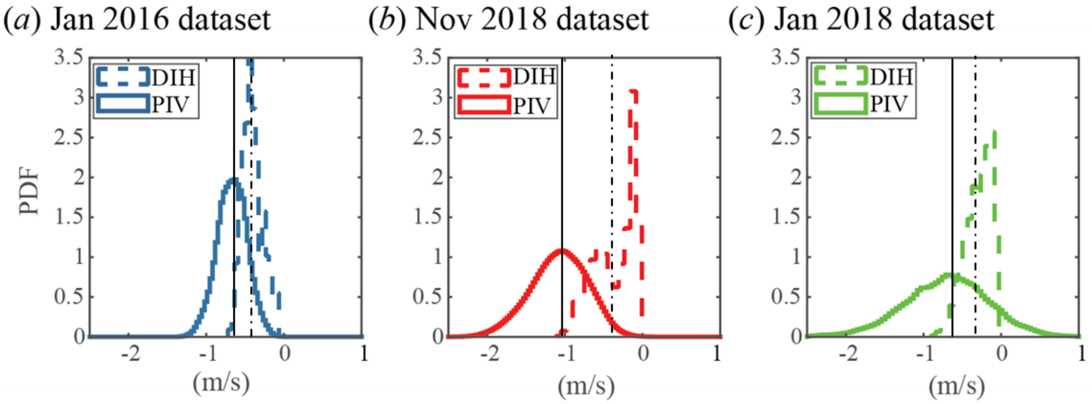

FIGURE 16. The PDFs of snow particle terminal (dashed line) from DIH analysis and settling velocity (solid line) from PIV analysis for (a) the Jan 2016 (solid blue line), (b) Nov 2018 (dotted red line), and (c) Jan 2019 (dashed green line) datasets.

Such a fall speed enhancement is interpreted as an effect of the particle-turbulence interaction. As mentioned in the introduction, the majority of previous numerical and experimental studies found that turbulence significantly enhances the settling velocity of small inertial particles by means of the preferential sweeping mechanism (Wang & Maxey 1994; Aliseda *et al*. 2002; Good *et al*. 2014; Ireland, Bragg & Collins 2016a; Rosa *et al.* 2016). In particular, the measurements of Aliseda *et al.* (2002) and Good *et al.* (2014) showed that droplets with *St* of order unity falling in air turbulence can reach settling velocities two to three times larger than in still air. Those experiments were conducted at Reynolds numbers one order of magnitude lower than the present one. Numerical studies have also been limited in Reynolds numbers and typically reported maximum settling enhancements of 30% to 80 %. Recent simulations covering wide parameter ranges suggest that settling enhancement is indeed stronger for higher turbulent dissipation rates (Ayala et al. 2008; Rosa *et al.* 2016) and larger Re_λ (Ireland *et al.* 2016a).

Deployment datasets	V_t (m/s)	W_s (m/s)	$W_s\ /V_t$
Jan 2016	0.40	0.67	1.68
Nov 2018	0.36	1.07	2.98
Jan 2019	0.30	0.70	2.33

TABLE 5. A summary of mean snow particle terminal velocity and snow settling velocity.

The present results may help to shed some light on longstanding questions on the relationship between snowflake size, morphology, fall speed, and turbulence. In fact, these results support the hypothesis that turbulence has a dominant role in determining not only the variance but also the mean of the snowflake settling velocity.

Chapter 5: Summary

We provide a systematic field investigation of snow settling dynamics with detailed characterization of snow and turbulence conditions. Using a holographic technique, a variety of individual snowflakes in nature are captured when they fall to the ground. Observations show that natural snow particles do not demonstrate near-perfect symmetry most of the time, and often have rough surfaces. Additionally, individual ice crystals often form aggregates with other crystals while they fall toward the surface of the earth.

We mostly focus on the effects of particle shapes on the fall velocity and determining the enhancement of mean settling velocity by turbulence. The hydrodynamic behaviors of six types of freely falling snowflakes are explored in this study. Flow characteristics, fall behavior, and an analysis of the results are reported, and are in general agreement with previous numerical studies and reported observations. Such information is important in accurately modeling snow precipitation under different weather conditions. In general, the result signifies that snow particles react to different turbulent intensities in a complex way, specifically depending on their inertial properties and on the turbulent spectrum.

Bibliography

- Aliseda, A., Cartellier, A., Hainaux, F., & Lasheras, J. C. (2002). Effect of preferential concentration on the settling velocity of heavy particles in homogeneous isotropic turbulence. Journal of Fluid Mechanics, 468, 77-105.
- Ayala, O., Rosa, B., Wang, L. P., & Grabowski, W. W. (2008). Effects of turbulence on the geometric collision rate of sedimenting droplets. Part 1. Results from direct numerical simulation. New Journal of Physics, 10(7), 075015.
- Ayyalasomayajula, S., Gylfason, A., Collins, L. R., Bodenschatz, E., & Warhaft, Z. (2006). Lagrangian measurements of inertial particle accelerations in grid generated wind tunnel turbulence. Physical Review Letters, 97(14), 144507.
- Bodenschatz, E., Malinowski, S. P., Shaw, R. A., & Stratmann, F. (2010). Can we understand clouds without turbulence. Science, 327(5968), 970-971.
- Böhm, H. P. (1989). A general equation for the terminal fall speed of solid hydrometeors. *Journal of the Atmospheric Sciences*, *46*(15), 2419-2427.
- Cox, E. P. (1927). A method of assigning numerical and percentage values to the degree of roundness of sand grains. Journal of Paleontology, 1(3), 179-183.
- Dasari, T., Wu, Y., Liu, Y., & Hong, J. (2019). Near-wake behaviour of a utility-scale wind turbine. Journal of Fluid Mechanics, 859, 204-246.
- Dioguardi, F., Mele, D., & Dellino, P. (2018). A new one-equation model of fluid drag for irregularly shaped particles valid over a wide range of Reynolds number. Journal of Geophysical Research: Solid Earth, 123(1), 144-156.
- Garrett, T. J., & Yuter, S. E. (2014). Observed influence of riming, temperature, and turbulence on the fallspeed of solid precipitation. Geophysical Research Letters, 41(18), 6515-6522.
- Good, G. H., Ireland, P. J., Bewley, G. P., Bodenschatz, E., Collins, L. R., & Warhaft, Z. (2014). Settling regimes of inertial particles in isotropic turbulence. Journal of Fluid Mechanics, 759.
- Haider, A., & Levenspiel, O. (1989). Drag coefficient and terminal velocity of spherical and nonspherical particles. Powder technology, 58(1), 63-70.

- Heymsfield, A. J., & Westbrook, C. D. (2010). Advances in the estimation of ice particle fall speeds using laboratory and field measurements. Journal of the Atmospheric Sciences, 67(8), 2469-2482.
- Higuchi, K. (1956). New method for the simultaneous observation of shape and size of a large number of falling snow particles. Journal of Meteorology, 13(3), 274-278.
- Högström, U., Hunt, J. C. R., & Smedman, A. S. (2002). Theory and measurements for turbulence spectra and variances in the atmospheric neutral surface layer. Boundary-Layer Meteorology, 103(1), 101-124.
- Hong, J., Toloui, M., Chamorro, L. P., Guala, M., Howard, K., Riley, S., ... & Sotiropoulos, F. (2014). Natural snowfall reveals large-scale flow structures in the wake of a 2.5-MW wind turbine. Nature communications, 5, 4216.
- Huang, N., Sang, J., & Han, K. (2011). A numerical simulation of the effects of snow particle shapes on blowing snow development. Journal of Geophysical Research: Atmospheres, 116(D22).
- Ireland, P. J., Bragg, A. D., & Collins, L. R. (2016). The effect of Reynolds number on inertial particle dynamics in isotropic turbulence. Part 1. Simulations without gravitational effects. Journal of Fluid Mechanics, 796, 617-658.
- Ireland, P. J., Bragg, A. D., & Collins, L. R. (2016). The effect of Reynolds number on inertial particle dynamics in isotropic turbulence. Part 2. Simulations with gravitational effects. Journal of Fluid Mechanics, 796, 659-711.
- Kubo, M., Seto, K., Muramoto, K., Fujiyoshi, Y., Shinoda, T., & Ohigashi, T. (2009, August). Shape classification of snow particle into snowflake and graupel using image processing. In 2009 ICCAS-SICE (pp. 5451-5456). IEEE.
- Langleben, M. P. (1954). The terminal velocity of snowflakes. Quarterly Journal of the Royal Meteorological Society, *80*(344), 174-181.
- Leinonen, J., & Berne, A. Unsupervised classification of snowflake images using a generative adversarial network and K-medoids classification.
- Libbrecht, K. G. (2007). The formation of snow crystals: subtle molecular processes govern the growth of a remarkable variety of elaborate ice structures. American Scientist, 95(1), 52-59.

- Libbrecht, K. G. (2017). Physical dynamics of ice crystal growth. Annual Review of Materials Research, 47, 271-295.
- Lim, S., Moisseev, D., Chandrasekar, V., & Lee, D. R. (2013). Classification and quantification of snow based on spatial variability of radar reflectivity. Journal of the Meteorological Society of Japan. Ser. II, 91(6), 763-774.
- Lin, Y., Donner, L. J., & Colle, B. A. (2011). Parameterization of riming intensity and its impact on ice fall speed using ARM data. Monthly Weather Review, 139(3), 1036-1047.
- Locatelli, J. D., & Hobbs, P. V. (1974). Fall speeds and masses of solid precipitation particles. Journal of Geophysical Research, 79(15), 2185-2197.
- Magono, C., & Lee, C. W. (1966). Meteorological classification of natural snow crystals. Journal of the Faculty of Science, Hokkaido University. Series 7, Geophysics, 2(4), 321-335.
- Marshall, J. S. (1953). Precipitation trajectories and patterns. Journal of Meteorology, 10(1), 25-29.
- Mason, B. J. (1994). The shapes of snow crystals—Fitness for purpose. Quarterly Journal of the Royal Meteorological Society, 120(518), 849-860.
- Maxey, M. R. (1987). The gravitational settling of aerosol particles in homogeneous turbulence and random flow fields. Journal of Fluid Mechanics, 174, 441-465.
- Mitchell, D. L. (1996). Use of mass-and area-dimensional power laws for determining precipitation particle terminal velocities. Journal of the atmospheric sciences, 53(12), 1710-1723.
- Mosimann, L., Weingartner, E., and Waldvogel, A.: An analysis of accreted drop sizes and mass on rimed snow crystals, J. Atmos. Sci., 51, 1548–1558, 1994.
- Nakaya, U., & Terada Jr, T. (1935). Simultaneous observations of the mass, falling velocity and form of individual snow crystals. 北海道帝國大學理學部紀要= Journal of the Faculty of Science, Hokkaido Imperial University. Ser. 2, Physics, 1(7), 191-200.

- Nakaya, U., & Sekido, Y. (1936). General classification of snow crystals and their frequency of occurrence. 北海道帝國大學理學部紀要= Journal of the Faculty of Science, Hokkaido Imperial University. Ser. 2, Physics, 1(9), 243-264.
- Nakaya, U. (1954). Snow crystal, natural and artificial. Harvard University Press.
- Nemes, A., Dasari, T., Hong, J., Guala, M., & Coletti, F. (2017). Snowflakes in the atmospheric surface layer: observation of particle–turbulence dynamics. Journal of Fluid Mechanics, 814, 592-613.
- Nettesheim, J. J., & Wang, P. K. (2018). A numerical study on the aerodynamics of freely falling planar ice crystals. Journal of the Atmospheric Sciences, 75(9), 2849-2865.
- Nielsen, P. (1993). Turbulence effects on the settling of suspended particles. Journal of Sedimentary Research, 63(5), 835-838.
- Praz, C., Roulet, Y. A., & Berne, A. (2017). Solid hydrometeor classification and riming degree estimation from pictures collected with a Multi-Angle Snowflake Camera. Atmospheric Measurement Techniques, 10(4), 1335.
- Pruppacher, H. R., & Klett, J. D. (1997). Microphysics of Clouds and Precipitation, Springer Publications.
- Rosa, B., Parishani, H., Ayala, O., & Wang, L. P. (2016). Settling velocity of small inertial particles in homogeneous isotropic turbulence from high-resolution DNS. International Journal of Multiphase Flow, 83, 217-231.
- Saddoughi, S. G., & Veeravalli, S. V. (1994). Local isotropy in turbulent boundary layers at high Reynolds number. Journal of Fluid Mechanics, 268, 333-372.
- Schaefer, V. J. (1947). Properties of particles of snow and the electrical effects they produce in storms. Eos, Transactions American Geophysical Union, 28(4), 587-614.
- Starr, D. O. C., & Cox, S. K. (1985). Cirrus clouds. Part I: A cirrus cloud model. Journal of the atmospheric sciences, 42(23), 2663-2681.
- Stull, R. B. (1988). Mean boundary layer characteristics. In An Introduction to Boundary Layer Meteorology (pp. 1-27). Springer, Dordrecht.

- Tran-Cong, S., Gay, M., & Michaelides, E. E. (2004). Drag coefficients of irregularly shaped particles. Powder Technology, 139(1), 21-32.
- Toloui, M., Riley, S., Hong, J., Howard, K., Chamorro, L. P., Guala, M., & Tucker, J. (2014). Measurement of atmospheric boundary layer based on super-large-scale particle image velocimetry using natural snowfall. Experiments in Fluids, 55(5), 1737.
- Tooby, P. F., Wick, G. L., & Isaacs, J. D. (1977). The motion of a small sphere in a rotating velocity field: a possible mechanism for suspending particles in turbulence. Journal of geophysical research, 82(15), 2096-2100.
- Tran-Cong, S., Gay, M., & Michaelides, E. E. (2004). Drag coefficients of irregularly shaped particles. Powder Technology, 139(1), 21-32.
- Wang, L. P., & Maxey, M. R. (1993). Settling velocity and concentration distribution of heavy particles in homogeneous isotropic turbulence. Journal of fluid mechanics, 256, 27-68.
- Wood, A. M., Hwang, W., & Eaton, J. K. (2005). Preferential concentration of particles in homogeneous and isotropic turbulence. International journal of multiphase flow, 31(10-11), 1220-1230.
- Zhang, R., Pitter, R. L., & Mitchell, D. L. (1989). Ground-based snowflake observations for analysis of orographic winter storms. In Papers Submitted to the Fifth WMO Scientific Conference on Weather Modification and Applied Cloud Physics: Beijing, China (8-12 May 1989). (Vol. 1, p. 47). Secretariat of the World Meteorological Organization.
- Zikmunda, J., & Vali, G. (1972). Fall patterns and fall velocities of rimed ice crystals. Journal of the Atmospheric Sciences, 29(7), 1334-1347.